

Pulsating with discrete symmetry

Alessandro Manacorda* and Étienne Fodor

Department of Physics and Materials Science, University of Luxembourg, L-1511 Luxembourg

(Dated: December 20, 2023)

We propose a class of diffusive lattice models where the internal states of particles are subject to a periodic drive. The discrete symmetry of states enforces an effective energy landscape which can counteract the drive to arrest the dynamics. Such a mechanism is reminiscent of the arrest reported in dense assemblies of pulsating deformable particles, in line with experiments in confluent biological tissues. We show that the competition between arrest and synchronisation promotes an instability which leads to spiral waves. Using analytical coarse-graining, we rationalize the emergence of such spirals in terms of a discrete gauge invariance at the hydrodynamic level.

Active matter describes non-equilibrium systems where a constant energy injection at the particle level leads to collective dynamics far from equilibrium, as is the case for many chemical, biological, and robotic systems [1–4]. In the last decades, most studies of active matter have focused on the role of self-propulsion, *i.e.* the ability of each particle to independently undergo directed motion. This paradigm has led to the theoretical understanding of several kinds of collective dynamics which have no counterpart in equilibrium systems [5, 6].

Interestingly, the energy injection in complex units need not result only into a self-propulsion mechanism. An important example is the case of deformable particles [7]. Indeed, complex aggregates such as macromolecules or living cells can change their shape due to internal activity [8], which leads to the spontaneous propagation of contraction waves in dense tissues. Such a wave propagation plays a crucial role in morphogenesis [9–14], uterine contraction [15, 16], and cardiac arrhythmogenesis [17, 18].

Vertex models are popular to capture the behavior of dense active systems such as biological tissues [19]. They typically consider self-propulsion as the only active component [20, 21]. Yet, when dense tissues behave like solids, it is questionable whether self-propulsion should be the key ingredient. Other models have considered dense assemblies of active deformable particles [22–27], where energy injection here occurs through the sustained oscillation of size at the single-particle level. With a Kuramoto-like synchronisation [28, 29] of particle sizes, contraction waves spontaneously emerge [26, 27], which are reminiscent of those reported in biological systems [13, 17].

Contraction waves in deformable active particles stem from the competition between synchronisation and steric repulsion [27]. The former favors a global cycling of particle sizes, while the latter promotes an arrested state without any cycling. Combining both stabilizes contraction waves. Interestingly, there are alternative mechanisms for arrest and synchronisation beyond steric repulsion and Kuramoto-like interactions. It remains to explore whether these alternatives lead to a phenomenology similar to that of deformable active particles. Indeed, one

may wonder whether the arrest-synchronisation competition actually is a generic scenario for pattern formation. If so, it encourages one to search for any hydrodynamic invariance and/or broken symmetry which might stand out as a hallmark of this competition.

In this Letter, we formulate a class of pulsating lattice models (PLM) featuring spiral waves with rotating defects [Fig. 1]. We reveal that the discrete symmetry of available states is key to arrest the dynamics, which, in combination with synchronisation and drive, generically yields wave propagation. Through analytical coarse-graining, we map PLM into a specific form of the complex Ginzburg-Landau equation (CGLE) [30] which breaks the *continuous* gauge invariance, while maintaining a *discrete* gauge invariance. We demonstrate how such an invariance not only signals the emergence of an arrested phase, but also constrains the features of the waves, at both the hydrodynamic and the particle-based

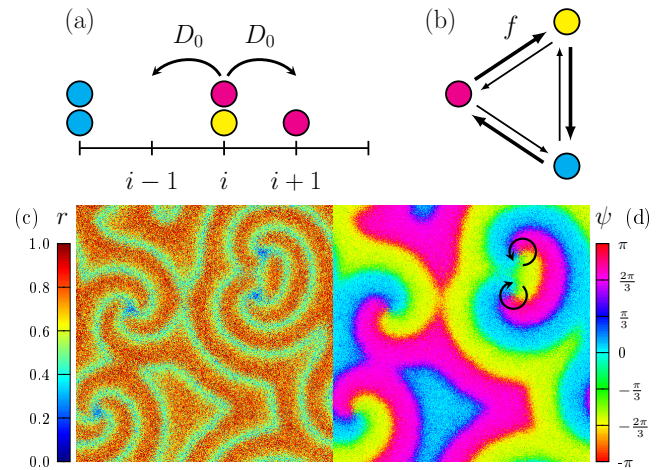


FIG. 1. (a) Particles freely diffuse without any volume exclusion. (b) Each particle is subject to an independent periodic driving which pulsates its internal state. Fully-connected onsite interactions locally synchronise the pulsation of particles. (c-d) Instabilities promote the coexistence of pulsating domains. Rotating defects appear at the meeting point of domain interfaces, thus forming spiral waves with a threefold symmetry. $(L, f, \varepsilon, D_0, \rho_0) = (512, 1.25, 2.5, 10^3, 10)$.

levels. Overall, the arrest-synchronisation competition in PLM provides a generic route for pattern formation, distinct from the well-studied instabilities in other models of reaction-diffusion systems (RDS) [31–33].

Pulsating lattice models.—We consider N particles in $V = L^d$ sites of a hypercubic d -dimensional lattice, with global number density $\rho_0 = N/V$, without any excluded volume. Each site contains an arbitrarily large number of particles. Each particle has an internal state, labeled by a discrete index $a \in \{1, \dots, q\}$, as a proxy to mimic the internal phase of deformable particles [22–27]. The crucial difference is that such states now feature a *discrete* symmetry. In what follows, we focus on the case $q = 3$, which is the minimal number of states to accommodate a current, and $d = 2$. The system configuration $\{n_{\mathbf{j},a}\}$ is then given by the number of particles for each state a and site \mathbf{j} .

At every time step dt/N , a particle with state a can either jump to a neighbouring site with probability $D_0 dt$, or switch to state b with probability $W_{ba} dt$ [Figs. 1(a,b)]:

$$W_{ba} = \exp \left[-f_{ba} + \frac{\varepsilon}{\rho_{\mathbf{j}}} (n_{\mathbf{j},b} - n_{\mathbf{j},a}) \right]. \quad (1)$$

The first term in the exponent of Eq. (1) is defined by $f_{ab} = \pm f$ when $a - b = \pm 1 \pmod{3}$, and $f_{ab} = 0$ otherwise. This drive mimics the pulsation of deformable active particles [22–27]. Inspired by some active lattice dynamics [34–40], the second term accounts for a synchronising Potts-like [41] interaction with strength ε , where $\rho_{\mathbf{j}} = \sum_a n_{\mathbf{j},a}$ is the local density at site \mathbf{j} . This term favors transition towards the state with the highest number of particles locally.

While interactions between particles are fully connected onsite, different sites exchange information only via diffusion. At small D_0 , many transitions of internal states occur in between two rare jumps of sites. At large D_0 , jumps are so frequent that now *all* particles are effectively interacting in between two state transitions. In both cases, patterns cannot emerge, and the system can be described solely in terms of the onsite dynamics [42, 43].

Synchronisation and arrest in the onsite case.—In the absence of diffusion ($D_0 = 0$), the evolution of the onsite occupation numbers n_a can be studied in terms of the complex parameter

$$A(t) = \frac{1}{\rho_0} \sum_{a=1}^3 e^{\frac{2\pi i}{3}a} n_a(t). \quad (2)$$

There are three stable phases [42, 43]: (i) a disordered phase at small ε , where particles are uniformly distributed in the three states, with symmetric fixed point $n_a = \rho_0/3$, and $|A|$ vanishes at large ρ_0 ; (ii) a cycling phase at intermediate ε , where particles collectively undergo periodic transitions between states; (iii) an arrested phase at large ε , with three asymmetric fixed

points $n_a \gg \rho_0/3$ invariant under the cyclic permutations $A \rightarrow A e^{\frac{2\pi i}{3}k}$ (k integer). Transitions between states can here be regarded as unimolecular reactions, in contrast with some models of multimolecular RDS [44, 45]. Besides, the total number of particles here is conserved. These features lead to stabilising disorder, and ensure that the arrest is not an absorbing phase.

In the cycling phase, the discrete nature of the internal states enforces that the global phase $\arg(A)$ is subject to an effective energy landscape. Indeed, the local extrema of the Potts-like interaction, at $\arg(A) = k\pi/3$, constrain the dynamics of the phase. While Kuramoto oscillators (with continuous symmetry) synchronously cycle without any cost, the collective transition of Potts oscillators (with discrete symmetry) between two nearby synchronised configurations implies crossing a desynchronised configuration, which is not energetically favored. Consequently, as ε increases, Potts oscillators spend more time in a given state before cycling to the next one. Above a critical ε , this energetic effect completely counteracts the drive, breaking down the periodicity of oscillations, and eventually stabilizing the arrested phase [46]. A similar phase trapping has been reported in clock models of aligning self-propelled particles [40].

In short, arrest emerges in PLM solely due to the discrete symmetry of internal states. Therefore, PLM entail a competition between arrest and synchronisation despite the absence of any volume exclusion, in contrast with models of continuously deformable particles [26, 27]. This competition opens the door to the emergence of dynamical patterns in spatially extended systems.

Spiral waves in the spatially extended case.—In the presence of diffusion ($D_0 > 0$), the displacement of particles follows a free dynamics, independently of any interaction, so that the density profile is always homogeneous. Yet, the spatial distribution of the particle states may not remain homogeneous. Indeed, even when particles are synchronised on site, they might not be synchronised between sites, so that the system can potentially accommodate spatial instabilities.

To study the emergence of dynamical patterns, we introduce the *local* complex parameter

$$A_{\mathbf{j}}(t) = \frac{1}{\rho_{\mathbf{j}}(t)} \sum_{a=1}^3 e^{\frac{2\pi i}{3}a} n_{\mathbf{j},a}(t) \equiv r_{\mathbf{j}}(t) e^{i\psi_{\mathbf{j}}(t)}. \quad (3)$$

When all particles are cycling in synchrony, the amplitude $r_{\mathbf{j}} \approx 1$ and the phase $\psi_{\mathbf{j}}$ are homogeneous. The period of $\psi_{\mathbf{j}}$ increases with ε , and eventually diverges. Before diverging, it undergoes large temporal fluctuations, which may desynchronise nearby sites, thus promoting spatial fluctuations of $\psi_{\mathbf{j}}$. At large D_0 , spatial fluctuations are suppressed by the rapid displacement of particles in the system. Instead, at moderate D_0 , such fluctuations can potentially build up into a large-scale instability.

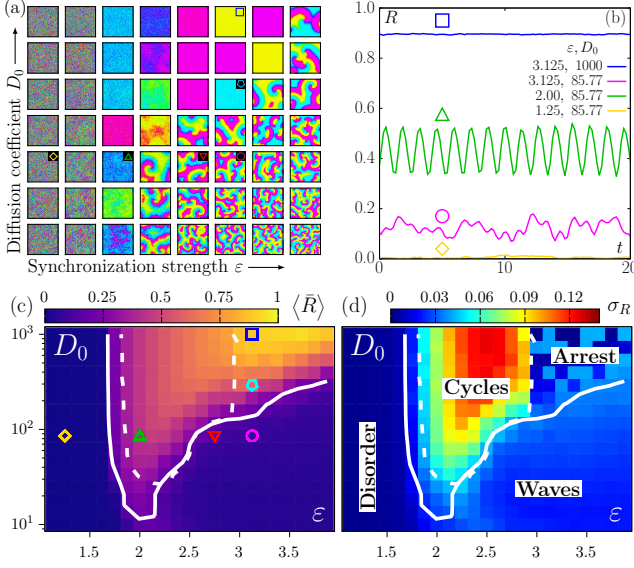


FIG. 2. (a) Snapshots of the local phase ψ_j [Eq. (3), color code in Fig. 1(d)]. (b) Trajectories of the synchronisation parameter $R(t)$ [Eq. (4)]. (c) The averaged parameter $\langle \bar{R} \rangle$ and (d) its standard deviation σ_R [Eq. (5)] lead to guidelines delineating boundaries between four phases. The solid and dashed lines correspond respectively to $\langle \bar{R} \rangle = 0.2$ and $\sigma_R = 0.045$. Symbols refer to the parameter values taken for panels (a-b) and Fig. 3. $(L, \rho_0) = (128, 10)$, and $f = \varepsilon/2$.

Instabilities can lead to the spatial coexistence of three cycling domains where $r_j \equiv r_{j,c} \approx 1$. Interfaces between domains have a finite width where $r_{j,c} > r_j > 0$. The meeting points of interfaces are given by defects where $r_j \approx 0$. Since all domains cycle at the same frequency, defects effectively rotate, thus forming spiral waves with a threefold symmetry [Figs. 1(c-d)]. Defects connected by the same interface rotate in opposite directions, and can annihilate by pair when colliding. Higher D_0 increases the domain sizes and interface widths, thus reducing the number of defects. Higher ε reduces the interface widths and increases $r_{j,c}$ [Fig. 2(a)].

Remarkably, we do not observe any phase with turbulent waves, in contrast with the case of continuously deformable particles [27]. Such a turbulence stems in [27] from excitations of the homogeneous arrested phase which promote some localized, aperiodic cyclings. The discrete symmetry of PLM, which entails three arrested states, prevents such events by trapping the phase before it completes one cycle. Therefore, waves in PLM spontaneously organize into steady spirals. Note that the merging of defects can actually also stabilize planar waves. Besides, when initially ordered, the system can also accommodate circular waves without any defect [46].

Phase boundaries and transitions.—In addition to the phase with waves, we also observe the emergence of three homogeneous phases (disorder, cycles, arrest) analogous to the onsite case. To quantitatively distinguish these

phases, we introduce the synchronisation parameter

$$R(t) = \frac{1}{N} \left| \sum_{j,a} e^{\frac{2\pi i}{3} a} n_{j,a}(t) \right|. \quad (4)$$

The trajectories of $R(t)$ allow us to identify four scenarios [Figs. 2(a,b)]: (i) a disordered phase at small ε [$R(t) \approx 0$, yellow line]; (ii) a cycling phase at intermediate ε and large D_0 [oscillating $R(t)$, green line]; (iii) an arrested phase at large ε and large D_0 [$R(t) \lesssim 1$, blue line]; (iv) spiral waves at large ε and intermediate D_0 [$R(t)$ strongly fluctuates, pink line].

To delineate phase boundaries, we consider the time-averaged \bar{R} and the variance σ_R^2 of $R(t)$ [Eq. (4)]:

$$\bar{R} = \int_{t_0}^{t_0+t} \frac{R(u) du}{t}, \quad \sigma_R^2 = \int_{t_0}^{t_0+t} \frac{\langle [R(u) - \bar{R}]^2 \rangle du}{t}, \quad (5)$$

where $\langle \cdot \rangle$ is an average over realizations. $\langle \bar{R} \rangle$ is clearly smaller in the disordered and wave phases (without global synchronisation) than in the cycling and arrested phases (with global synchronisation) [Fig. 2(c)]. The variance σ_R is higher in the cycling phase than in all others [Fig. 2(d)]. Indeed, $R(t)$ strongly oscillates in this phase [Fig. 2(b)], due to the periodic desynchronisation between two nearby synchronised states (see discussion above on Potts oscillators). Altogether, $\langle \bar{R} \rangle$ and σ_R allow us to draw phase boundaries.

We examine how the distribution $P(R)$ varies across transitions [Fig. 3]. Deep in the wave and arrested phases [resp. pink and dark blue lines], $P(R)$ has a single peak, respectively at small and large R . Deep in the cycling phase [green line], $P(R)$ is nonzero for a finite domain of R and peaks at its boundaries, due to the oscillations of $R(t)$. Going from waves to arrest, $P(R)$ becomes bimodal, thus signalling metastability [Fig. 3(a)]. Similarly, going from waves to cycling, $P(R)$ is now nonzero in two separated domains, due to the coexistence between the two dynamical states [Fig. 3(b)]. In short, both the arrest-wave and cycling-wave transitions feature a metastable regime.

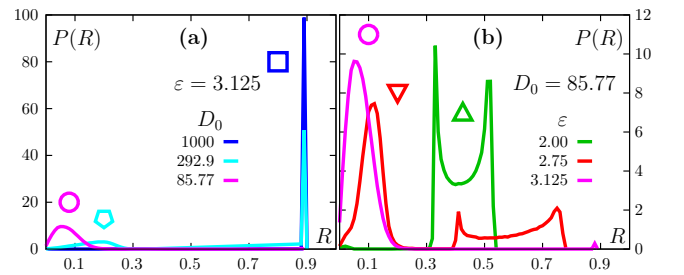


FIG. 3. Probability density of the synchronisation parameter R [Eq. (4)] across the phase boundaries in Fig. 2. (a) The arrested-wave transition and (b) the cycling-wave transition both display a regime of metastability. Distribution measured over 1024 realizations.

Gauge invariance in the hydrodynamics.—Although spiral waves have been already reported in many RDS, one may wonder how the patterns in Figs. 1(c-d) actually differ from standard instabilities present, for instance, in the CGLE [30]. To address this question, we coarse-grain PLM in terms of $A_j(t) \rightarrow \mathcal{A}(\mathbf{x}, t)$ in the continuum limit. Neglecting density fluctuations, and expanding to lowest orders in \mathcal{A} , we get

$$\begin{aligned} \partial_t \mathcal{A} &= D \nabla^2 \mathcal{A} + \mathcal{L}(\mathcal{A}) + \Lambda, \\ \mathcal{L}(\mathcal{A}) &= c_1 \mathcal{A} + c_2 \mathcal{A}^{*2} + c_3 |\mathcal{A}|^2 \mathcal{A}, \end{aligned} \quad (6)$$

where $*$ refers to complex conjugation, Λ is a zero-mean Gaussian white noise, $D \propto D_0$ is the macroscopic diffusion coefficient, and (c_1, c_2, c_3) are complex coefficients fixed by (f, ε) [46]. The \mathcal{A}^{*2} term in Eq. (6) breaks the continuous gauge $\mathcal{A} \rightarrow \mathcal{A} e^{i\phi}$, in contrast with the standard CGLE [30]. Yet, this term preserves the discrete gauge $\mathcal{A} \rightarrow \mathcal{A} e^{\frac{2\pi i}{q} k}$, in contrast with the hydrodynamics of continuously deformable particles [27]. To the third order in \mathcal{A} , Eq. (6) actually contains all the terms compatible with this gauge.

The local hydrodynamics $\partial_t \mathcal{A} = \mathcal{L}(\mathcal{A})$ reproduces the three homogeneous phases of PLM (disorder, cycles, and arrest) stemming from the interplay between the active drive and the energy landscape [Figs. 4(a-c)]. The breakdown of the continuous gauge ensures the existence of the arrested phase, as in [27]. The discrete gauge enforces that the local hydrodynamics can actually arrest in either one of three states, at variance with [27]. This degeneracy directly affects the shape of the hydrodynamic patterns. Indeed, Eq. (6) entails an instability promoting the spatial coexistence of cycling domains. Rotating defects with threefold symmetry spontaneously form where interfaces meet [Figs. 4(d-e)], yielding the same spiral waves as in PLM [Figs. 1(c-d)].

In short, our coarse-graining shows that PLM are not captured by the standard CGLE [30], and therefore differ from standard RDS. It is striking that, although our hydrodynamics is an expansion at small \mathcal{A} , the lowest-order nonlinearities are here sufficient to reproduce the specific shape of particle-based spirals. Through the discrete gauge invariance, these nonlinearities bear the hallmark of the microscopic discrete symmetry.

Discussion.—We reveal that PLM entail spiral waves stemming from the competition between arrest and synchronisation. Therefore, our results show that the arrest-synchronisation scenario for pattern formation [27] extends to a broad class of models with discrete symmetry. Such a symmetry suffices to promote arrest, thus providing a mechanism distinct from that of repulsive deformable particles [27]. Waves are shaped by the discrete gauge invariance at the hydrodynamic level, which distinguishes them from the patterns of other RDS [31–33].

Our work paves the way to examining the interplay between discrete symmetry and pattern formation for

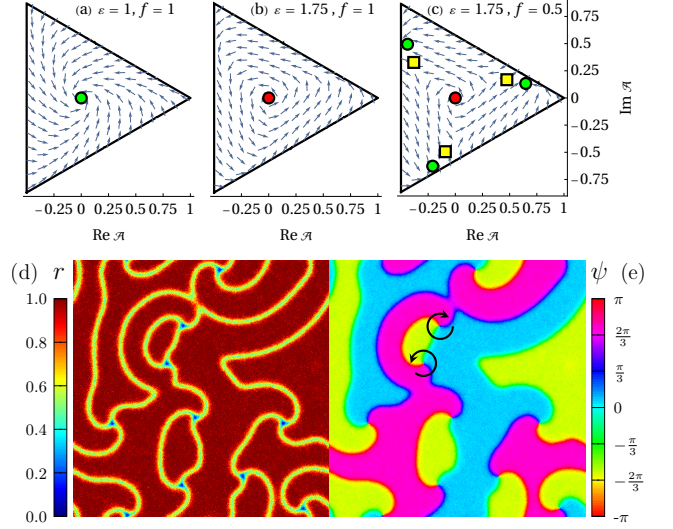


FIG. 4. Stream plot of the local hydrodynamics $\partial_t \mathcal{A} = \mathcal{L}(\mathcal{A})$ [Eq. (6)] for (a) disorder, (b) cycles, and (c) arrest. Symbols indicate stable fixed points (green circles), unstable fixed points (red circles), and saddles (yellow squares). (d-e) Spiral waves centered around rotating defects spontaneously form in the hydrodynamics, analogously to the patterns in PLM [Figs. 1(c-d)]. $(L, f, \varepsilon, D, \rho_0) = (512, 0.5, 2.5, 100, 10)$.

arbitrary q . Indeed, we expect that the three homogeneous phases (disorder, cycles, arrest) are robust beyond $q = 3$. To study patterns, one can use a top-down approach postulating the hydrodynamics by identifying the terms which obey the discrete gauge $\mathcal{A} \rightarrow \mathcal{A} e^{\frac{2\pi i}{q} k}$. As in our coarse-graining [46], one can also derive the hydrodynamic coefficients in terms of the microscopic parameters. It is tempting to speculate that, depending on the parity of q , such a hydrodynamic study could lead to identifying generic properties of defect dynamics, and potential connections with the topology of other active models [47].

The discrete symmetry of PLM seems to preclude defect turbulence, at variance with the standard CGLE [30] and its recent generalization [27]. To capture such a turbulence, one could introduce energy levels which maintain the discrete nature of PLM while breaking its symmetry. The arrested phase would no longer be degenerate, thus opening the door to local excitations nucleating defects from a homogeneous phase, as reported in [27]. In this context, it would be interesting to explore how density fluctuations affect defect nucleation, at both the hydrodynamic and the particle-based levels.

We acknowledge fruitful discussions with L. K. Davis, M. Esposito, J. Meibom, and Y. Zhang. This project has received funding from the European Union's Horizon Europe research and innovation programme under the Marie Skłodowska-Curie grant agreement No 101056825 (NewGenActive), and from the Luxembourg National

Research Fund (FNR), grant reference 14389168.

* alessandro.manacorda@uni.lu

- [1] T. Vicsek and A. Zafeiris, Collective motion, *Phys. Rep.* **517**, 71 (2012).
- [2] M. C. Marchetti, J. F. Joanny, S. Ramaswamy, T. B. Liverpool, J. Prost, M. Rao, and R. A. Simha, Hydrodynamics of soft active matter, *Rev. Mod. Phys.* **85**, 1143 (2013).
- [3] C. Bechinger, R. Di Leonardo, H. Löwen, C. Reichhardt, G. Volpe, and G. Volpe, Active particles in complex and crowded environments, *Rev. Mod. Phys.* **88**, 045006 (2016).
- [4] É Fodor and M.C. Marchetti, The statistical physics of active matter: From self-catalytic colloids to living cells, *Physica A* **504**, 106 (2018).
- [5] M. E. Cates and J. Tailleur, Motility-induced phase separation, *Annu. Rev. Condens. Matter Phys.* **6**, 219 (2015).
- [6] H. Chaté, Dry aligning dilute active matter, *Annu. Rev. Condens. Matter Phys.* **11**, 189 (2020).
- [7] M. L. Manning, Essay: Collections of deformable particles present exciting challenges for soft matter and biological physics, *Phys. Rev. Lett.* **130**, 130002 (2023).
- [8] S. Zehnder, M. Suaris, M. Bellaire, and T. Angelini, Cell volume fluctuations in mdck monolayers, *Biophys. J.* **108**, 247 (2015).
- [9] J. Solon, A. Kaya-Çopur, J. Colombelli, and D. Brunner, Pulsed forces timed by a ratchet-like mechanism drive directed tissue movement during dorsal closure, *Cell* **137**, 1331 (2009).
- [10] A. C. Martin, M. Kaschube, and E. F. Wieschaus, Pulsed contractions of an actin-myosin network drive apical constriction, *Nature* **457**, 495 (2009).
- [11] G. B. Blanchard, S. Murugesu, R. J. Adams, A. Martinez-Arias, and N. Gorfinkel, Cytoskeletal dynamics and supracellular organisation of cell shape fluctuations during dorsal closure, *Development* **137**, 2743 (2010).
- [12] K. Kruse and D. Rivelin, Chapter three - spontaneous mechanical oscillations: Implications for developing organisms, in *Forces and Tension in Development*, Current Topics in Developmental Biology, Vol. 95, edited by M. Labouesse (Academic Press, 2011) pp. 67–91.
- [13] X. Serra-Picamal, V. Conte, R. Vincent, E. Anon, D. T. Tambe, E. Bazellieres, J. P. Butler, J. J. Fredberg, and X. Trepat, Mechanical waves during tissue expansion, *Nat. Phys.* **8**, 628 (2012).
- [14] C.-P. Heisenberg and Y. Bellaïche, Forces in tissue morphogenesis and patterning, *Cell* **153**, 948 (2013).
- [15] J. Xu, S. N. Menon, R. Singh, N. B. Garnier, S. Sinha, and A. Pumir, The role of cellular coupling in the spontaneous generation of electrical activity in uterine tissue, *PLOS ONE* **10**, 1 (2015).
- [16] K. M. Myers and D. Elad, Biomechanics of the human uterus, *Wiley Interdiscip. Rev. Syst. Biol. Med.* **9**, e1388 (2017).
- [17] A. Karma, Physics of cardiac arrhythmogenesis, *Annu. Rev. Condens. Matter Phys.* **4**, 313 (2013).
- [18] S. Alonso, M. Bär, and B. Echebarria, Nonlinear physics of electrical wave propagation in the heart: a review, *Rep. Prog. Phys.* **79**, 096601 (2016).
- [19] T. Nagai and H. Honda, A dynamic cell model for the formation of epithelial tissues, *Philos. Mag. B* **81**, 699 (2001).
- [20] D. Bi, J. H. Lopez, J. M. Schwarz, and M. L. Manning, A density-independent rigidity transition in biological tissues, *Nat. Phys.* **11**, 1074 (2015).
- [21] D. Bi, X. Yang, M. C. Marchetti, and M. L. Manning, Motility-driven glass and jamming transitions in biological tissues, *Phys. Rev. X* **6**, 021011 (2016).
- [22] E. Tjhung and T. Kawasaki, Excitation of vibrational soft modes in disordered systems using active oscillation, *Soft Matter* **13**, 111 (2017).
- [23] E. Tjhung and L. Berthier, Discontinuous fluidization transition in time-correlated assemblies of actively deforming particles, *Phys. Rev. E* **96**, 050601 (2017).
- [24] C. Brito, E. Lerner, and M. Wyart, Theory for swap acceleration near the glass and jamming transitions for continuously polydisperse particles, *Phys. Rev. X* **8**, 031050 (2018).
- [25] N. Oyama, T. Kawasaki, H. Mizuno, and A. Ikeda, Glassy dynamics of a model of bacterial cytoplasm with metabolic activities, *Phys. Rev. Res.* **1**, 032038 (2019).
- [26] Y. Togashi, Modeling of nanomachine/micromachine crowds: Interplay between the internal state and surroundings, *J. Phys. Chem. B* **123**, 1481 (2019).
- [27] Y. Zhang and E. Fodor, Pulsating active matter, *Phys. Rev. Lett.* **131**, 238302 (2023).
- [28] Y. Kuramoto, *Chemical Oscillations, Waves, and Turbulence* (Springer Berlin Heidelberg, 1984).
- [29] J. A. Acebrón, L. L. Bonilla, C. J. Pérez Vicente, F. Ritort, and R. Spigler, The Kuramoto model: A simple paradigm for synchronization phenomena, *Rev. Mod. Phys.* **77**, 137 (2005).
- [30] I. S. Aranson and L. Kramer, The world of the complex ginzburg-landau equation, *Rev. Mod. Phys.* **74**, 99 (2002).
- [31] J. D. Murray, ed., *Mathematical Biology I: An Introduction* (Springer New York, 2002).
- [32] J. D. Murray, ed., *Mathematical Biology II: Spatial models and biomedical applications* (Springer New York, 2003).
- [33] G. Ódor, Universality classes in nonequilibrium lattice systems, *Rev. Mod. Phys.* **76**, 663 (2004).
- [34] A. G. Thompson, J. Tailleur, M. E. Cates, and R. A. Blythe, Lattice models of nonequilibrium bacterial dynamics, *J. Stat. Mech.: Theory Exp.* **2011** (02), P02029.
- [35] A. P. Solon and J. Tailleur, Revisiting the flocking transition using active spins, *Phys. Rev. Lett.* **111**, 078101 (2013).
- [36] A. P. Solon and J. Tailleur, Flocking with discrete symmetry: The two-dimensional active ising model, *Phys. Rev. E* **92**, 042119 (2015).
- [37] A. Manacorda and A. Puglisi, Lattice model to derive the fluctuating hydrodynamics of active particles with inertia, *Phys. Rev. Lett.* **119**, 208003 (2017).
- [38] A. Manacorda, *Lattice Models for Fluctuating Hydrodynamics in Granular and Active Matter* (Springer, 2018).
- [39] M. Kourbane-Houssene, C. Erignoux, T. Bodineau, and J. Tailleur, Exact hydrodynamic description of active lattice gases, *Phys. Rev. Lett.* **120**, 268003 (2018).
- [40] A. Solon, H. Chaté, J. Toner, and J. Tailleur, Susceptibility of polar flocks to spatial anisotropy, *Phys. Rev.*

- Lett. **128**, 208004 (2022).
- [41] F. Y. Wu, The potts model, *Rev. Mod. Phys.* **54**, 235 (1982).
 - [42] T. Herpich, J. Thingna, and M. Esposito, Collective power: Minimal model for thermodynamics of nonequilibrium phase transitions, *Phys. Rev. X* **8**, 031056 (2018).
 - [43] T. Herpich and M. Esposito, Universality in driven potts models, *Phys. Rev. E* **99**, 022135 (2019).
 - [44] T. Reichenbach, M. Mobilia, and E. Frey, Mobility promotes and jeopardizes biodiversity in rock–paper–scissors games, *Nature* **448**, 1046 (2007).
 - [45] T. Reichenbach, M. Mobilia, and E. Frey, Self-organization of mobile populations in cyclic competition, *J. Theor. Biol.* **254**, 368 (2008).
 - [46] See supplemental material at [URL_will_be_inserted_by_publisher](#), which includes Refs. [48–50].
 - [47] S. Shankar, A. Souslov, M. J. Bowick, M. C. Marchetti, and V. Vitelli, Topological active matter, *Nat. Rev. Phys.* **4**, 380–398 (2022).
 - [48] O. Tange, *GNU parallel 2018* (Lulu.com, 2018).
 - [49] C. W. Gardiner, *Stochastic methods: a handbook for the natural and social sciences*, Vol. 4 (Springer, 2009).
 - [50] W. Liu and U. C. Täuber, Nucleation of spatiotemporal structures from defect turbulence in the two-dimensional complex ginzburg-landau equation, *Phys. Rev. E* **100**, 052210 (2019).

Supplemental material: Pulsating with discrete symmetry

Alessandro Manacorda* and Étienne Fodor

Department of Physics and Materials Science, University of Luxembourg, L-1511 Luxembourg

(Dated: December 20, 2023)

S1. SIMULATION OF MICROSCOPIC LATTICE DYNAMICS

Simulations are performed on a square lattice in $d = 2$ dimensions. Every particle is labeled with a state $a \in \{1, \dots, q\}$, with $q = 3$ from now on. The microscopic configuration of the system is given by the positions $\mathbf{i}_n \in \{1, L\}^2$ and states σ_n of each particle $n \in \{1, \dots, N\}$ at a given discrete time $t = sdt/N$. The system is invariant under relabelling of particles, which preserves the occupation numbers

$$n_{\mathbf{j},a} = \sum_{n=1}^N \delta_{\mathbf{i}_n, \mathbf{j}} \delta_{\sigma_n, a} , \quad (\text{S1})$$

accounting for the number of particles at site \mathbf{j} with state a . The microscopic configuration at discrete time s is then univocally determined by the occupation numbers. The lattice size is $V = L^2$ and the number of particles is $N = \rho_0 V$. Simulations are performed with $L = 128$ in the phase diagram shown in Fig. 2(c-d) of the main text, and $L = 512$ in Fig. 1(c-d); $\rho_0 = 10$ in both cases.

At every time step, a particle n is chosen with uniform random distribution $p_n = 1/N$, and a uniform number $\xi \in [0, 1]$ is drawn to decide whether (i) the particle jumps to a next-neighbor site with probability $D_0 dt$, (ii) the particle switches from state a to state b with probability $W_{ba} dt$, or (iii) none of the above with probability $1 - (2dD_0 + \sum_{b \neq a} W_{ba}) dt$. To ensure normalization, the last term must be positive; the time step dt is then taken as

$$dt = [2dD_0 + e^{f+\varepsilon} + e^{-f}]^{-1} \lesssim \left(2dD_0 + \max_{\{n\}} \sum_{b \neq a} W_{ba} \right)^{-1} , \quad (\text{S2})$$

assuming $\varepsilon > 0$ as usual. After each move, the time is advanced by dt/N , so that each particle attempts a move on average once at each $t \rightarrow t + dt$ [1]. Simulations have been performed via the ULHPC cluster and parallelised with the use of GNU parallel [2]. Snapshots in Fig. 1(c-d) and phase diagrams of Fig. 2(c-d) of the main text are realised with 128 realizations starting from initially disordered configurations, i.e. every particle's position and state are independent and drawn from a uniform distribution. Realizations are performed until $t_{\max} = 200$ in our system, and statistical measures (averages and standard deviations) are performed in the time window $t_0 < t < t_{\max}$, where $t_0 = 150$, consisting of 256 measures. The phase boundaries in Fig. 2(c-d) of the main text are drawn via a linear interpolation of the raw data, thus locating the isosurfaces of constant $\langle \bar{R} \rangle$ or σ_R . The dynamics shown in the snapshots in Fig. 1(c-d) of the main text can be found in the video `Lattice.mp4`.

A. Transition from cycles to arrest in the onsite dynamics ($D_0 = 0$)

We report in Fig. S1 the transition from cycles to arrest for the onsite dynamics mentioned in the main text. The arrested fixed points are given by the asymmetric stationary solutions of the master equation

$$\dot{n}_a = \sum_{b(\neq a)} [W_{ab}(\mathbf{n}) n_b - W_{ba}(\mathbf{n}) n_a] . \quad (\text{S3})$$

At small ε , the phase oscillates with a periodic behavior [purple line in Fig. S1], whereas the phase arrests at large ε [cyan line in Fig. S1]. In between these regimes, fluctuations can lead to escape from arrest, so that the phase ψ spend a large random time close to a fixed point, before a random event allows it to continue cycling [green line in Fig. S1].

* alessandro.manacorda@uni.lu

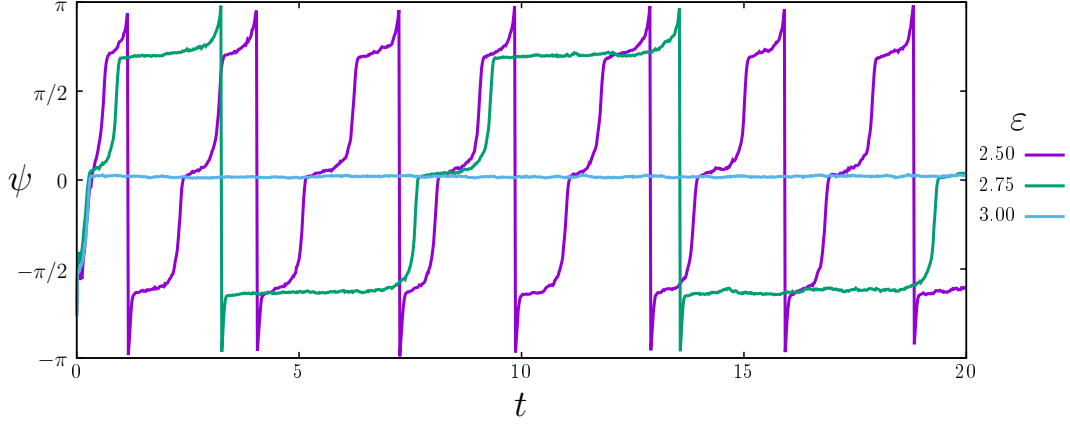


FIG. S1. Transition from cycle to arrest in the onsite dynamics: $N = 1000$ particles with drive $f = 2$ evolve on a single-site, i.e. $D_0 = 0$. At $\varepsilon = 2.5$ (purple line), the system is in a cycling state where the phase ψ oscillates. Increasing ε , the oscillations slow down ($\varepsilon = 2.75$, green line), and higher synchronisation leads to arrest, i.e. $\dot{\psi} \sim 0$ when $\varepsilon = 3.0$ (cyan line).

B. Wave propagation with ordered initial conditions

The spiral wave propagation described in the main text takes place when the system is quenched from a disordered initial condition. Instead, when the initial condition is ordered, the homogeneous ordered state is destabilized by nucleation of droplets. This behavior is shown in Fig. S2. At $t = 10$, the system is ordered and homogeneous with $\psi(\mathbf{x}) \simeq 0$. At $t = 15$, small droplets with $\psi \simeq 2\pi/3$ are visible. At $t = 20$ more droplets have formed and the previous ones are expanding. At $t = 25, 30$, droplets merge and the state $\psi \simeq 2\pi/3$ invades the system. At $t = 35$, the state $\psi \simeq 0$ has almost disappeared; a droplet with $\psi \simeq -2\pi/3$ is visible in the top left region, starting again the nucleation destabilizing the homogeneous profile $\psi(\mathbf{x}) \simeq 2\pi/3$.

C. Interface width and domain size

During wave propagation, higher synchronisation sharpens the interfaces between domains, and higher diffusion increases the domains' size. This effect is visible in Fig. S3. Both effects have an energetic motivation: interfaces correspond to intermediate synchronisation at the saddle points of the underlying energetic landscape, and are therefore penalized by higher synchronisation. Diffusion allows particles to interact over higher length scales, leading to larger domains. Diffusion thus entails a characteristic length scale $l = \sqrt{D\tau}$, related to characteristic times of the dynamics such as pulsation $\tau_f = \cosh f$ or nucleation time τ_{nuc} . When this length scale is comparable with the system size ($l \sim L$) the system becomes homogeneous.

S2. DERIVATION OF HYDRODYNAMICS

A. Coarse-graining the microscopic lattice dynamics

The microscopic dynamics of occupation numbers in discrete time reads

$$n_{\mathbf{i},a,s+1} = n_{\mathbf{i},a,s} + J_{\mathbf{i},a,s}, \quad (\text{S4})$$

being $J_{\mathbf{i},a,s} = 0, \pm 1$ the increment of species a at site \mathbf{i} and time step s . Following the procedure in [3] we derive the hydrodynamic equations from the equation above by writing the probability of a single trajectory $\{n_{\mathbf{i},a,s}\}$ for $a = 0, 1, 2$, $\mathbf{i} \in \Lambda$ and $s = 0, \dots, T/dt$, which reads

$$\mathbb{P}[\{n_{\mathbf{i},a,s}\}] = \left\langle \prod_{\mathbf{i},s,a} \delta(n_{\mathbf{i},a,s+1} - n_{\mathbf{i},a,s} - J_{\mathbf{i},a,s}) \right\rangle_{\mathbf{J}}, \quad (\text{S5})$$

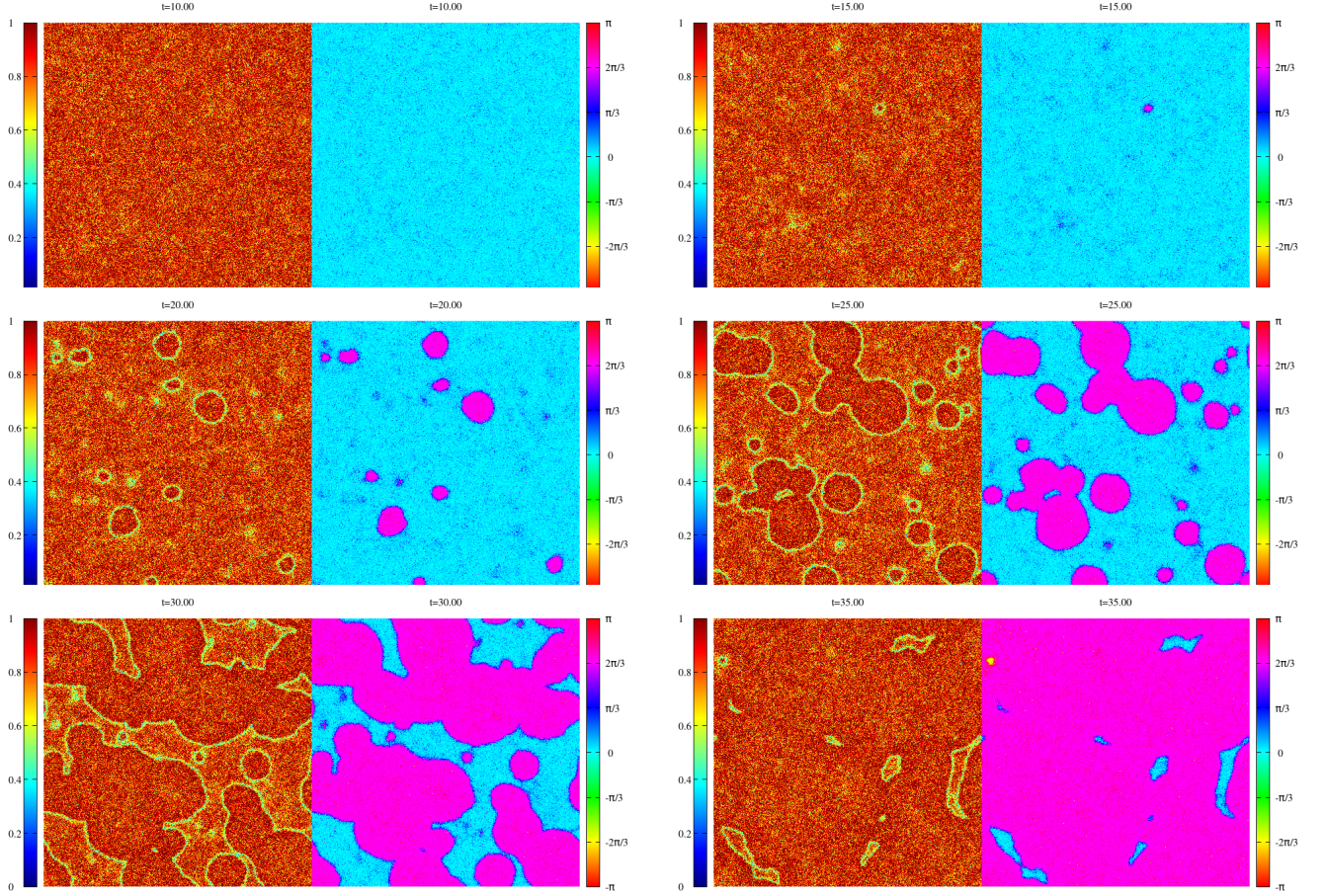


FIG. S2. Nucleation and expansion of stable states destabilizing the arrested homogeneous state. Phase-amplitude plots, respectively r (left panels) and ψ (right panels) shown as in Fig. 1(c-d) of the main text, for $10 < t < 35$ (times are shown in the plot titles). Parameters: $(L, f, \varepsilon, D_0, \rho_0) = (512, 1.5, 3, 10^2, 10)$.

being $\langle \cdot \rangle_{\mathbf{J}}$ the average over the possible realizations of $\mathbf{J} = \{J_{i,a,s}\}$. Expanding the delta functions in their integral representation we have

$$\mathbb{P}[\{n_{i,a,s}\}] = \int \prod_{i,s,a} \left(d\hat{n}_{i,a,s} e^{\hat{n}_{i,a,s}(n_{i,a,s+1} - n_{i,a,s})} \langle e^{-\hat{n}_{i,a,s} J_{i,a,s}} \rangle_{\mathbf{J}} \right). \quad (\text{S6})$$

The last term must be computed looking at the microscopic probabilities defined in the main text. At a given time p , we have the following options:

- a jump from site \mathbf{i} to site $\mathbf{i} + \sigma \mathbf{e}_\mu$, being $\sigma = \pm 1$ and \mathbf{e}_μ the unit vector in the μ -th direction, occurring with probability $D_0 dt$, yielding $J_{i,a,s} = -1$ and $J_{i+\sigma \mathbf{e}_\mu, a, s} = +1$;
- a transition from state a to state b on the site \mathbf{i} , occurring with probability $W_{ba}(\bar{n}_{i,a,s})$, yielding $J_{i,a,s} = -1$ and $J_{i,b,s} = +1$;
- a null event, occurring with probability $1 - \sum_{i,a} (2dD_0 + \sum_b W_{ba}) dt$.

In the definition above, we indicate with $\bar{n}_{i,a,s}$ the occupation numbers involved in the transition rates, which can in principle refer to neighboring sites (not necessarily nearest-neighbors), as in [3]. In this work transition rates are computed at zero-range, i.e. taking into account only particles in the same site, but we keep the derivation general

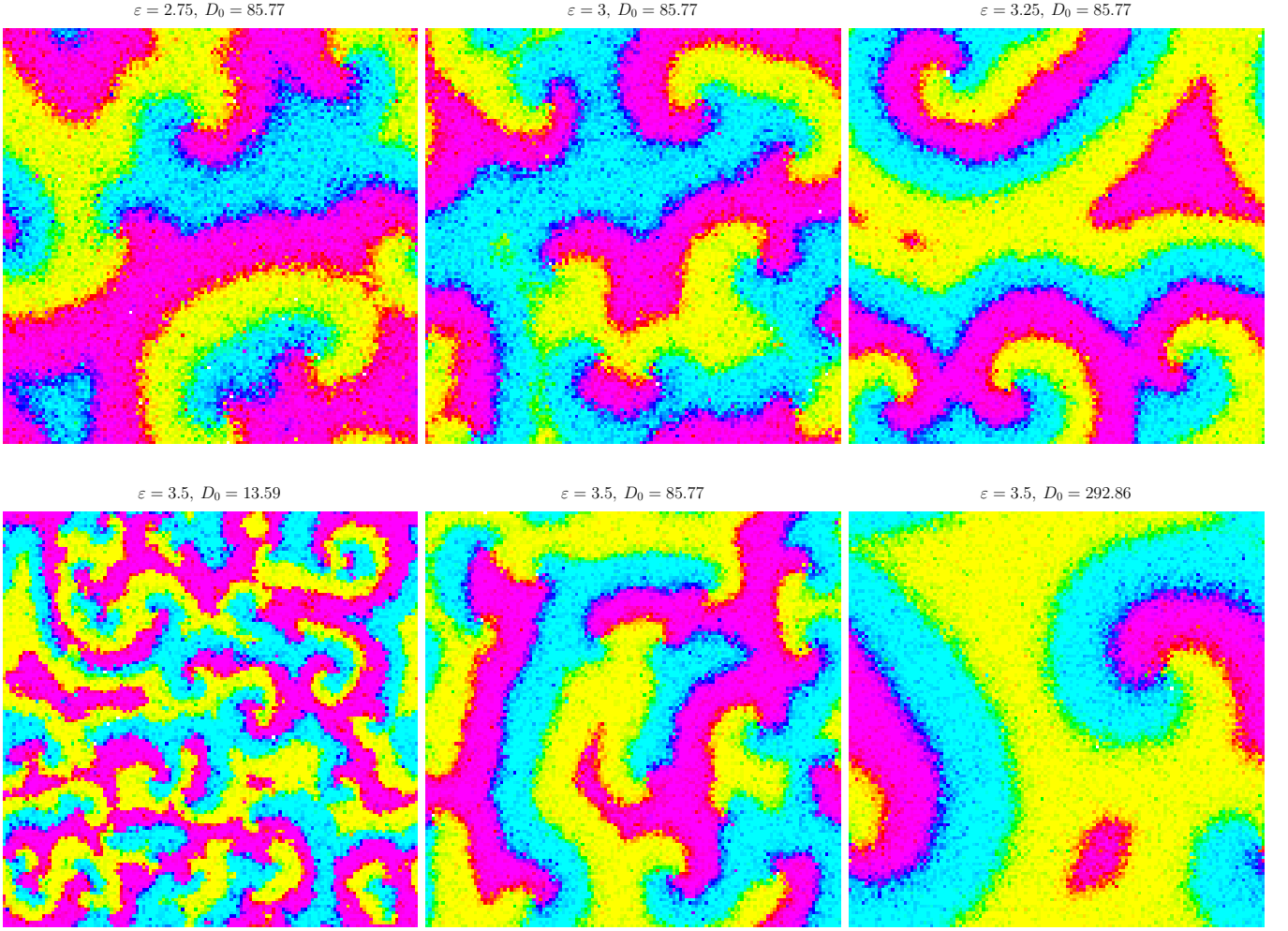


FIG. S3. Snapshots of the phase field in the wave regime to illustrate the effect of synchronisation and diffusion. Top panels: synchronisation increases from left to right. Interfaces between domains become more regular as fluctuations are suppressed by strong coupling. Bottom panel: diffusion increases from left to right. Higher diffusion leads to larger domains. Parameters: $(L, f, \rho_0) = (128, \varepsilon/2, 10)$.

to facilitate further work. We can therefore write the average over \mathbf{J} as

$$\begin{aligned}
 \prod_{\mathbf{i},a} \langle e^{-\hat{n}_{\mathbf{i},a,s} J_{\mathbf{i},a,s}} \rangle_{\mathbf{J}} &\simeq 1 + \sum_{\mathbf{i},a} \sum_{\mu,\sigma} (e^{\hat{n}_{\mathbf{i},a,s} - \hat{n}_{\mathbf{i}+\sigma\mathbf{e}_{\mu},a,s}} - 1) n_{\mathbf{i},a,s} D_0 dt + \sum_{\mathbf{i},a} \sum_b (e^{\hat{n}_{\mathbf{i},a,s} - \hat{n}_{\mathbf{i},b,s}} - 1) n_{\mathbf{i},a,s} W_{ba}(\bar{\mathbf{n}}_{\mathbf{i},s}) dt \\
 &\simeq \prod_{\mathbf{i},a} \exp \left\{ \sum_{\mu} [(e^{\hat{n}_{\mathbf{i},a,s} - \hat{n}_{\mathbf{i}+\mathbf{e}_{\mu},a,s}} - 1) n_{\mathbf{i},a,s} + (e^{\hat{n}_{\mathbf{i}+\mathbf{e}_{\mu},a,s} - \hat{n}_{\mathbf{i},a,s}} - 1) n_{\mathbf{i}+\mathbf{e}_{\mu},a,s}] D_0 dt \right. \\
 &\quad \left. + \sum_b (e^{\hat{n}_{\mathbf{i},a,s} - \hat{n}_{\mathbf{i},b,s}} - 1) n_{\mathbf{i},a,s} W_{ba}(\bar{\mathbf{n}}_{\mathbf{i},s}) dt \right\}. \tag{S7}
 \end{aligned}$$

We inject the last result in Eq. (S6), and consider the continuous-time limit through the substitutions:

$$n_{\mathbf{i},a,s+1} - n_{\mathbf{i},a,s} \rightarrow \dot{n}_{\mathbf{i},a} dt ; \quad \sum_{s=1}^{T/dt} dt \rightarrow \int_0^T dt ; \quad \prod_s d\hat{n}_{\mathbf{i},a,s} \rightarrow \mathcal{D}\hat{n}_{\mathbf{i},a} , \tag{S8}$$

so that the probability of a trajectory reads

$$\mathbb{P}[\{n_{\mathbf{i},a}(t)\}] = \int \prod_{\mathbf{i},a} \mathcal{D}\hat{n}_{\mathbf{i},a} e^{-S[\mathbf{n},\hat{\mathbf{n}}]} , \tag{S9}$$

with

$$S = - \int_0^T dt \sum_{\mathbf{i},a} \left\{ \hat{n}_{\mathbf{i},a} \dot{n}_{\mathbf{i},a} + D_0 \sum_{\mu} \left[(e^{\hat{n}_{\mathbf{i},a} - \hat{n}_{\mathbf{i}+\mathbf{e}_{\mu},a}} - 1) n_{\mathbf{i},a} + (e^{\hat{n}_{\mathbf{i}+\mathbf{e}_{\mu},a} - \hat{n}_{\mathbf{i},a}} - 1) n_{\mathbf{i}+\mathbf{e}_{\mu},a} \right] \right. \\ \left. + \sum_b (e^{\hat{n}_{\mathbf{i},a} - \hat{n}_{\mathbf{i},b}} - 1) n_{\mathbf{i},a} W_{ba}(\bar{\mathbf{n}}_{\mathbf{i}}) \right\}. \quad (\text{S10})$$

The continuous-space limit can be taken by introducing the lattice spacing λ and substituting

$$n_{\mathbf{i},a} \rightarrow \lambda^d \rho_a(\mathbf{x}); \quad \hat{n}_{\mathbf{i},a} \rightarrow \hat{\rho}_a(\mathbf{x}); \quad \sum_{\mathbf{i} \in \Lambda} \rightarrow \int_{V=[0;\ell]^d} d\mathbf{x} \lambda^{-d}; \quad \nabla_{\mathbf{i},\mu} \rightarrow \lambda \frac{\partial}{\partial x_{\mu}} + \frac{1}{2} \lambda^2 \frac{\partial^2}{\partial x_{\mu}^2}, \quad (\text{S11})$$

being $\ell = L\lambda$ the lattice length and $\nabla_{\mathbf{i},\mu} f_{\mathbf{i}} \equiv f_{\mathbf{i}+\mathbf{e}_{\mu}} - f_{\mathbf{i}}$ the μ -th coordinate of the discrete gradient. After summing over the coordinates μ , the leading order in the Taylor expansion of the action reads

$$S = S_0 + \mathcal{O}(\lambda) = - \int_0^T dt \int_V d\mathbf{x} \sum_a \left[\hat{\rho}_a \dot{\rho}_a + D (|\nabla \hat{\rho}_a|^2 \rho_a + \nabla \rho_a \cdot \nabla \hat{\rho}_a) + \sum_b (e^{\hat{\rho}_a - \hat{\rho}_b} - 1) \rho_a W_{ba}(\bar{\rho}) \right] + \mathcal{O}(\lambda), \quad (\text{S12})$$

having defined $D = D_0 \lambda^2 = \mathcal{O}(1)$ in the hydrodynamic limit $\lambda \rightarrow 0$, $\ell = \mathcal{O}(1)$. To proceed further, we truncate the exponential of response fields at second order, which corresponds to an approximation of Gaussian noise for the fluctuating hydrodynamics. The action then reads

$$S_0 = - \int_0^T dt \int_V d\mathbf{x} \sum_a \left\{ \hat{\rho}_a \dot{\rho}_a + D (|\nabla \hat{\rho}_a|^2 \rho_a + \nabla \rho_a \cdot \nabla \hat{\rho}_a) + \sum_b \left[\hat{\rho}_a - \hat{\rho}_b + \frac{1}{2} (\hat{\rho}_a - \hat{\rho}_b)^2 \right] \rho_a W_{ba}(\bar{\rho}) \right\} \\ = - \int_0^T dt \int_V d\mathbf{x} \sum_a \left\{ \hat{\rho}_a \dot{\rho}_a + D (|\nabla \hat{\rho}_a|^2 \rho_a + \nabla \rho_a \cdot \nabla \hat{\rho}_a) + \hat{\rho}_a \sum_b [W_{ba}(\bar{\rho}) \rho_a - W_{ab}(\bar{\rho}) \rho_b] \right. \\ \left. + \frac{1}{2} \sum_{b(>a)} (\hat{\rho}_a - \hat{\rho}_b)^2 [W_{ba}(\bar{\rho}) \rho_a + W_{ab}(\bar{\rho}) \rho_b] \right\}. \quad (\text{S13})$$

The quadratic terms in the response fields can be removed through a Hubbard-Stratonovich transformation introducing the auxiliary fields $\xi_a(\mathbf{x}, t)$ (vectorial in space) and $\eta_{ab}(\mathbf{x}, t)$, so that (after integration by parts)

$$\mathbb{P}[\rho(\mathbf{x}, t)] = \frac{1}{Z} \int \mathcal{D}[\hat{\rho}_a, \xi_a, \eta_{ab}] e^{-S_0[\rho, \hat{\rho}, \xi, \eta]}, \\ S_0 = - \int_0^T dt \int_V d\mathbf{x} \sum_a \left\{ \hat{\rho}_a \dot{\rho}_a - \frac{1}{2} \xi_a^2 - \hat{\rho}_a \left[\nabla \cdot \left(\sqrt{2D\rho_a} \xi_a \right) + D \nabla^2 \rho_a \right] \right. \\ \left. + \hat{\rho}_a \sum_b [W_{ba}(\bar{\rho}) \rho_a - W_{ab}(\bar{\rho}) \rho_b] + \sum_{b(>a)} \left[-\frac{1}{2} \eta_{ab}^2 + \sqrt{W_{ba}(\bar{\rho}) \rho_a + W_{ab}(\bar{\rho}) \rho_b} (\hat{\rho}_a - \hat{\rho}_b) \eta_{ab} \right] \right\}. \quad (\text{S14})$$

In the last line, the noise terms η_{ab} are white and Gaussian; however, if we want to integrate over $\mathcal{D}\hat{\rho}_a$ in the first equation, we need to collect the terms separately. We thus define for $a < b$ the antisymmetric matrix Δ_{ab} and the noise field η_a as

$$\Delta_{ab}(\bar{\rho}) = \sqrt{W_{ba}(\bar{\rho}) \rho_a + W_{ab}(\bar{\rho}) \rho_b} = -\Delta_{ba}(\bar{\rho}), \quad \eta_a = \sum_{b(\neq a)} \Delta_{ab} \eta_{ba} \quad (\text{S15})$$

so that

$$\sum_{a < b} \Delta_{ab} (\hat{\rho}_a - \hat{\rho}_b) \eta_{ab} = \sum_a \eta_a \hat{\rho}_a, \\ \langle \xi_{a\mu}(\mathbf{x}, t) \xi_{bv}(\mathbf{x}', t') \rangle = \delta_{ab} \delta_{\mu\nu} \delta(\mathbf{x} - \mathbf{x}') \delta(t - t'), \\ \langle \eta_a(\mathbf{x}, t) \eta_b(\mathbf{x}', t') \rangle = \left[\delta_{ab} \sum_c \Delta_{ac}^2(\bar{\rho}(\mathbf{x}, t)) - (1 - \delta_{ab}) \Delta_{ab}^2(\bar{\rho}(\mathbf{x}, t)) \right] \delta(\mathbf{x} - \mathbf{x}') \delta(t - t'). \quad (\text{S16})$$

We rewrite the action further as

$$S_0 = - \int_0^T dt \int_V d\mathbf{x} \sum_a \left\{ \hat{\rho}_a \left[\dot{\rho}_a - \nabla \cdot \left(\sqrt{2D\rho_a} \boldsymbol{\xi}_a \right) - D\nabla^2 \rho_a - \sum_b (W_{ab}(\bar{\rho})\rho_b - W_{ba}(\bar{\rho})\rho_a) - \eta_a \right] - \frac{1}{2} \xi_a^2 - \sum_{b(>a)} \frac{1}{2} \eta_{ab}^2 \right\} . \quad (\text{S17})$$

Integrating over the response fields $\hat{\rho}_a$, we obtain

$$\mathbb{P}[\boldsymbol{\rho}(\mathbf{x}, t)] \propto \int \mathcal{D}[\xi_a, \eta_{ab}] e^{-\int dt dx \sum_a (\xi_a^2/2 + \sum_b \eta_{ab}^2/2)} \times \prod_a \delta \left(\dot{\rho}_a - \nabla \cdot \left(\sqrt{2D\rho_a} \boldsymbol{\xi}_a \right) - D\nabla^2 \rho_a - \sum_b (W_{ab}(\bar{\rho})\rho_b - W_{ba}(\bar{\rho})\rho_a) - \eta_a \right) , \quad (\text{S18})$$

yielding the fluctuating hydrodynamic (FHD) equations:

$$\dot{\rho}_a = -\nabla \cdot \mathbf{J}_a + T_a , \quad \mathbf{J}_a = -D\nabla \rho_a + \sqrt{2D\rho_a} \boldsymbol{\xi}_a , \quad T_a = \sum_b [W_{ab}(\bar{\rho})\rho_b - W_{ba}(\bar{\rho})\rho_a] + \eta_a . \quad (\text{S19})$$

We operate the linear change of variables leading us to the density field ρ and to the complex order parameter \mathcal{A}

$$\rho(\mathbf{x}, t) = \sum_a \rho_a(\mathbf{x}, t) , \quad \mathcal{A}(\mathbf{x}, t) = \frac{1}{\rho(\mathbf{x}, t)} \sum_a e^{\frac{2\pi i}{q} a} \rho_a(\mathbf{x}, t) . \quad (\text{S20})$$

The FHD equations become then

$$\begin{aligned} \partial_t \rho &= -\nabla \cdot \mathbf{J} , \quad \mathbf{J} = -D\nabla \rho + \sqrt{2D\rho} \boldsymbol{\xi} , \quad \boldsymbol{\xi} = \sum_a \sqrt{\rho_a/\rho} \boldsymbol{\xi}_a , \\ \partial_t (\rho \mathcal{A}) &= -\nabla \cdot \mathbf{J}_A + T_A , \quad \mathbf{J}_A = -D\nabla (\rho \mathcal{A}) + \sqrt{2D\rho} \boldsymbol{\xi}_A , \quad \boldsymbol{\xi}_A = \sum_a e^{\frac{2\pi i}{q} a} \sqrt{\rho_a/\rho} \boldsymbol{\xi}_a , \\ \left\langle (\xi_\mu, \xi_{A,\mu}, \xi_{A,\mu}^*)^\dagger (\mathbf{x}, t) (\xi_\nu, \xi_{A,\nu}, \xi_{A,\nu}^*) (\mathbf{x}', t') \right\rangle &= \begin{pmatrix} 1 & \mathcal{A} & \mathcal{A}^* \\ \mathcal{A}^* & 1 & \mathcal{A} \\ \mathcal{A} & \mathcal{A}^* & 1 \end{pmatrix} \delta_{\mu\nu} \delta(\mathbf{x} - \mathbf{x}') \delta(t - t') , \quad (\text{S21}) \\ T_A &= \sum_{ab} e^{\frac{2\pi i}{q} a} [W_{ab}(\bar{\rho})\rho_b - W_{ba}(\bar{\rho})\rho_a] + \eta_A , \\ \eta_A &= \sum_a e^{\frac{2\pi i}{q} a} \eta_a = \sum_{ab} e^{\frac{2\pi i}{q} a} \Delta_{ab} \eta_{ba} . \end{aligned}$$

The Δ_{ab} terms explicitly read

$$\begin{aligned} \Delta_{01}^2 &= \frac{2}{3} \rho \left[\cosh \Omega_1 + e^{-i\pi/3} \mathcal{A} \cosh (\Omega_1 + i\pi/3) + e^{i\pi/3} \mathcal{A}^* \cosh (\Omega_1 - i\pi/3) \right] , \quad \Omega_1 = f - \frac{\varepsilon}{\sqrt{3}} \left(e^{i\pi/6} \mathcal{A} + e^{-i\pi/6} \mathcal{A}^* \right) , \\ \Delta_{02}^2 &= \frac{2}{3} \rho \left[\cosh \Omega_2 + e^{i\pi/3} \mathcal{A} \cosh (\Omega_2 + i\pi/3) + e^{-i\pi/3} \mathcal{A}^* \cosh (\Omega_2 - i\pi/3) \right] , \quad \Omega_2 = f + \frac{\varepsilon}{\sqrt{3}} \left(e^{-i\pi/6} \mathcal{A} + e^{i\pi/6} \mathcal{A}^* \right) , \\ \Delta_{12}^2 &= \frac{2}{3} \rho [\cosh \Omega_3 - i\mathcal{A} \sinh (\Omega_3 - i\pi/6) + i\mathcal{A}^* \sinh (\Omega_3 + i\pi/6)] , \quad \Omega_3 = f + \frac{\varepsilon}{\sqrt{3}} i (\mathcal{A} - \mathcal{A}^*) . \end{aligned} \quad (\text{S22})$$

B. Expansion around the disordered state

We expand the hydrodynamic equations (S21) around the fixed point $\mathcal{A} = 0$, assuming $|\mathcal{A}| \ll 1$. Then, since the evolution of ρ does not depend on \mathcal{A} , the density relaxes to an homogeneous profile with Gaussian fluctuations around $\rho = \rho_0$. We then neglect current fluctuations (which can be interpreted as a large-size limit $L \gg 1$) and replace

$\rho(x, t)$ with a constant value ρ_0 in the equations for \mathcal{A} . We expand the transition rates in T_A up to the third order in $(\mathcal{A}, \mathcal{A}^*)$, following a Landau-Ginzburg scheme. We therefore get

$$\frac{1}{\rho_0} T_A \simeq c_1 \mathcal{A} + c_2 \mathcal{A}^{*2} + c_3 |\mathcal{A}|^2 \mathcal{A} + \frac{1}{\rho_0} \eta_A , \quad (\text{S23})$$

where

$$c_1 = (2\varepsilon - 3) \cosh f + i\sqrt{3} \sinh f , \quad c_2 = \varepsilon \left(\cosh f + i \frac{\varepsilon - 3}{\sqrt{3}} \sinh f \right) , \quad c_3 = \frac{\varepsilon^2}{6} \left[(2\varepsilon - 9) \cosh f + i\sqrt{3} \sinh f \right] . \quad (\text{S24})$$

This result sets a first condition for our expansion: one must have $\varepsilon < 9/2$ to avoid the divergence of the complex field. The noise can also be expanded noting that, when $\mathcal{A} = \mathcal{A}^* = 0$, one has from Eq. (S22)

$$\begin{aligned} \langle \eta_A(\mathbf{x}, t) \eta_A^*(\mathbf{x}', t') \rangle &= \left[6\rho_0 \cosh f + \mathcal{O}(\mathcal{A}) \right] \delta(\mathbf{x} - \mathbf{x}') \delta(t - t') , \\ \langle \eta_A(\mathbf{x}, t) \eta_A(\mathbf{x}', t') \rangle &= \langle \eta_A^*(\mathbf{x}, t) \eta_A^*(\mathbf{x}', t') \rangle = \mathcal{O}(\mathcal{A}) \delta(\mathbf{x} - \mathbf{x}') \delta(t - t') . \end{aligned} \quad (\text{S25})$$

Keeping only the first-order additive terms in the noise, one finds the hydrodynamics in Eq. (6) of the main text:

$$\begin{aligned} \partial_t \mathcal{A} &= D \nabla^2 \mathcal{A} + c_1 \mathcal{A} + c_2 \mathcal{A}^{*2} + c_3 |\mathcal{A}|^2 \mathcal{A} + \Lambda , \\ \langle \Lambda(\mathbf{x}, t) \Lambda^*(\mathbf{x}', t') \rangle &= \frac{6}{\rho_0} \cosh f \delta(\mathbf{x} - \mathbf{x}') \delta(t - t') , \\ \langle \Lambda(\mathbf{x}, t) \Lambda(\mathbf{x}', t') \rangle &= \langle \Lambda^*(\mathbf{x}, t) \Lambda^*(\mathbf{x}', t') \rangle = 0 . \end{aligned} \quad (\text{S26})$$

The CGLE global invariance $\mathcal{A} \rightarrow \mathcal{A} e^{i\varphi}$ is explicitly broken by the term \mathcal{A}^{*2} , yet the C_3 discrete symmetry $\mathcal{A} \rightarrow \mathcal{A} e^{\frac{2\pi i}{3} k}$ holds. The noiseless on-site dynamics in the phase-amplitude coordinates $\mathcal{A} = r e^{i\psi}$ with $\rho_0 = 1$ reads

$$\begin{aligned} \dot{r} &= a_1 r + |c_2| \cos(\varphi_2 - 3\psi) r^2 + a_3 r^3 , \\ r \dot{\psi} &= b_1 r + |c_2| \sin(\varphi_2 - 3\psi) r^2 + b_3 r^3 , \end{aligned} \quad (\text{S27})$$

where $c_j = a_j + i b_j$ and $c_2 = |c_2| e^{i\varphi_2}$. The fixed points of Eq. (S27) can be found as

$$|c_3|^2 r^4 + (c_1 \bar{c}_3 + \bar{c}_1 c_3 - |c_2|^2) r^2 + |c_1|^2 = 0 , \quad \tan(\varphi_2 - 3\psi) = \frac{b_1 + b_3 r^2}{a_1 + a_3 r^2} . \quad (\text{S28})$$

For the choice of the coefficients c_j in Eq. (S24), then Eq. (S28) admits two solutions (r_{\pm}, ψ_{\pm}) . We remark that the angle ψ is multiplied by 3 in both equations; this means that any fixed point ψ_{\pm} entails two symmetric fixed points with $r'_{\pm} = r_{\pm}$, $\psi'_{\pm} = \psi_{\pm} \pm 2\pi/3$, as a consequence of the discrete symmetry of the system. We follow two particular solutions in the $(-\pi, \pi]$ range, acknowledging that the symmetric solutions always exist. The fixed points (r_{\pm}, ψ_{\pm}) in the (ε, f) plane are shown in Fig. S4. The numerical analysis of linear stability proves that (r_+, ψ_+) is stable within almost all the existence region, except for a small area close to $f = 0$, $\varepsilon = 9/2$ which is beyond the physical domain of our equations. Conversely, the fixed point (r_-, ψ_-) is always unstable. Therefore the dynamics in the physical region always converges to (ρ_{\pm}, ψ_{\pm}) , when it exists.

These fixed points represent the ordered, arrested solution of the dynamics. We therefore observe three regions:

1. A region of stability of the disordered phase $\varepsilon < 3/2$.
2. A region of existence and stability of the ordered phase, shown in Fig. S4, leading to arrest.
3. A region where no fixed point is stable, leading to limit cycles since $\dot{\psi} \neq 0$.

The region in Fig. S4 defines a critical line $f_c(\varepsilon)$, and the ordered solution exists for $f < f_c(\varepsilon)$. Above $\varepsilon = 3$ one has $df_c/d\varepsilon < 0$: this behavior is not physical as we know that higher synchronisation should always promote order. We therefore take $\varepsilon = 3$ as an upper bound of the validity domain of our approximation. At the same time, the ordered fixed points exist only below the drive threshold $f_c(\varepsilon = 3) = \tanh^{-1}(1/\sqrt{2}) \simeq 0.88$, above which order cannot be achieved for any synchronisation strength. We furthermore remark that, in the same region $\varepsilon > 3$, there are solutions with $r > 1$ which have to be considered spurious as well - as from our definition in the main one always needs to have $0 \leq r \leq 1$. Therefore, the physical domain of validity of the third-order expansion is $|f| < f_c(3)$ and $0 < \varepsilon < 3$. This region is shown by the dashed black line in Fig. S4

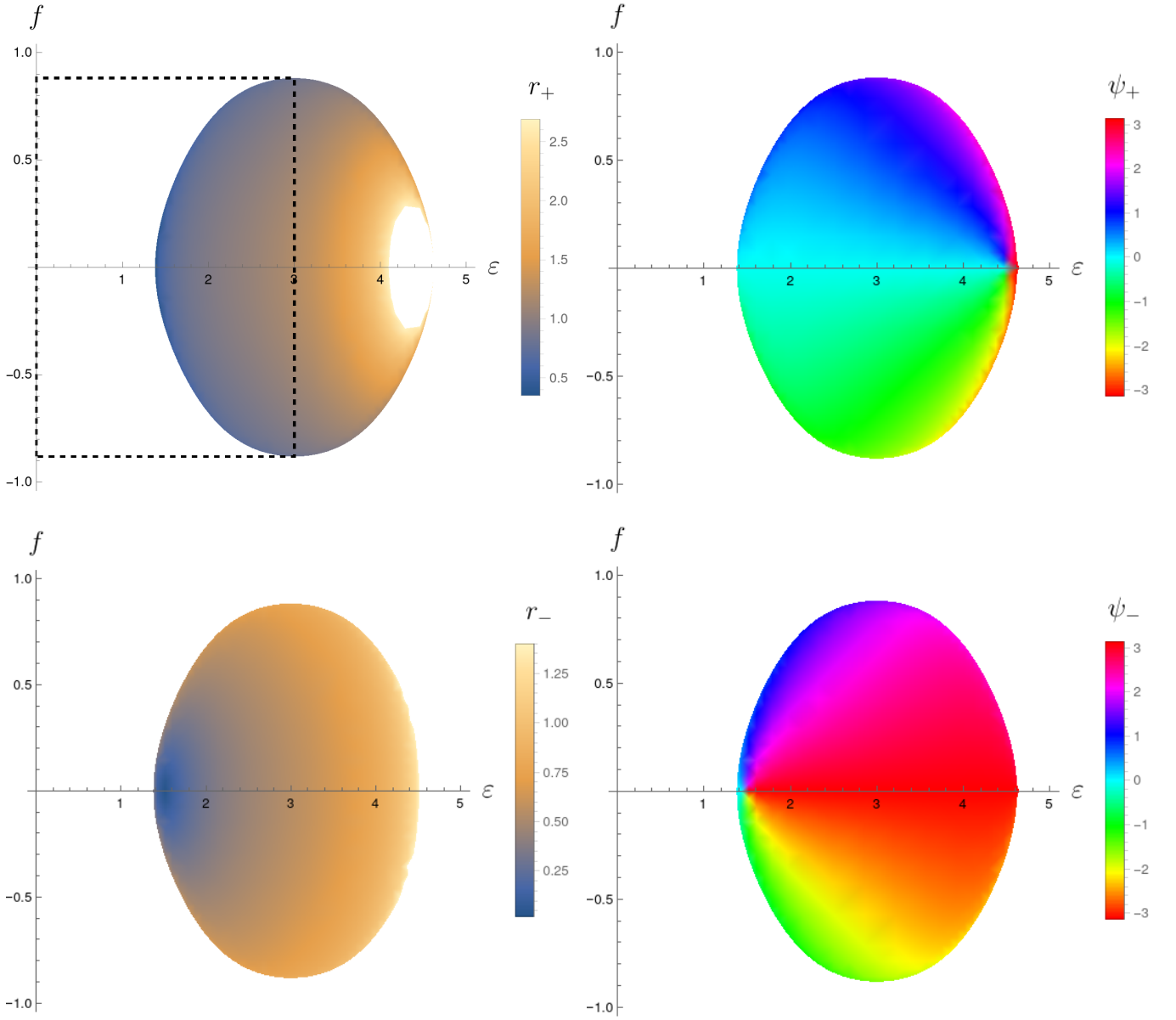


FIG. S4. The two ordered fixed points (r_{\pm}, ψ_{\pm}) of Eq. (S27) in the synchronisation-frequency plane. The dashed rectangle in top left panel shows the physical domain of validity of the hydrodynamics.

C. Simulation of hydrodynamic equations

Eqs. (S26) are simulated with a spectral method to treat the (linear) diffusion term. We simulate the equations in the range $(x, y) \in [0 : \ell]^2$ and $t > 0$, and perform a linear discretisation of space and time, namely $(x, y) = (i, j)\Delta x$ and $t = n\Delta t$, with $\Delta x = L/\ell = 1$ and $\Delta t = 10^{-3}$, being now L the number of spatial nodes. Simulations start from a disordered configuration, taking $A_{ij,n=0} = A_0(\xi_R + i\xi_I)$, being $\xi_{R/I}$ two Gaussian unitary random numbers. The discrete evolution $t \rightarrow t + \Delta t$ occurs in the following steps:

1. the local evolution is performed with a fourth-order Runge-Kutta scheme on the deterministic part, and the noise is added within the Euler-Maruyama scheme [4]. The Runge-Kutta scheme, even if not needed when noise is present, makes the discretisation robust also in the zero-noise limit [5]. The local fields are evolved as $A_{ij,n} \rightarrow A_{ij,n+1/2}$;
2. the evolved field is Fourier transformed and we get $\hat{A}_{hk,n+1/2} = \text{FFT}[A_{n+1/2}]$;

3. the modes $(h, k) \in \{-L/2, \dots, L/2 - 1\}^2$ are evolved locally taking into account only the diffusive term with a trapezoidal integration over the interval $[t, t + \Delta t]$, i.e.

$$\hat{A}_{hk,n+1} = \frac{1 - q^2 D \Delta t / 2}{1 + q^2 D \Delta t / 2} \hat{A}_{hk,n+1/2} \quad (\text{S29})$$

being $q^2 = \left(\frac{2\pi}{\ell}\right)^2 (h^2 + k^2)$;

4. the Fourier modes are antitransformed and we obtain the evolved complex field $A_{ij,n+1} = \text{FFT}^{-1}[\hat{A}_{n+1}]$.

The dynamics shown in the snapshots in Fig. 4(d-e) of the main text can be found in the video `Hydro.mp4`.

-
- [1] M. Kourbane-Houssene, C. Erignoux, T. Bodineau, and J. Tailleur, [Phys. Rev. Lett. **120**, 268003 \(2018\)](#).
 - [2] O. Tange, *GNU parallel 2018* (Lulu.com, 2018).
 - [3] A. G. Thompson, J. Tailleur, M. E. Cates, and R. A. Blythe, [J. Stat. Mech.: Theory Exp. **2011** \(02\), P02029](#).
 - [4] C. W. Gardiner, *Stochastic methods: a handbook for the natural and social sciences*, Vol. 4 (Springer, 2009).
 - [5] W. Liu and U. C. Täuber, [Phys. Rev. E **100**, 052210 \(2019\)](#).